

# Asymmetric Elimination Reaction on Chiral Metal Surfaces

Samuel Stolz, Martina Danese, Marco Di Giovannantonio, José I. Urgel, Qiang Sun, Amogh Kinikar, Max Bommert, Shantanu Mishra, Harald Brune, Oliver Gröning, Daniele Passerone, and Roland Widmer\*

The production of enantiopure materials and molecules is of uttermost relevance in research and industry in numerous contexts, ranging from nonlinear optics to asymmetric synthesis. In the context of the latter, dehalogenation, which is an essential reaction step for a broad class of chemical reactions, is investigated; specifically, dehalogenation of prochiral 5-bromo-7-methylbenz(a)anthracene (BMA) on prototypical, chiral, intermetallic PdGa{111} surfaces under ultrahigh vacuum conditions. Asymmetric halogen elimination is demonstrated by combining temperature-programmed X-ray photoelectron spectroscopy, scanning probe microscopy, and density functional theory. On the PdGa{111} surfaces, the difference in debromination temperatures for the two BMA surface enantiomers amounts up to an unprecedented 46 K. The significant dependence of the dehalogenation temperature of the BMA surface enantiomers on the atomic termination of the PdGa{111} surfaces implies that the ensemble effect is pronounced in this reaction step. These findings evidence enantiospecific control and hence promote intrinsically chiral crystals for asymmetric on-surface synthesis.

## 1. Introduction

The inherent homochirality of biomolecules, such as proteins or polysaccharides, and the consequential enantiospecific interactions with other chiral molecules evoke a need for the production of enantiopure compounds. Accordingly, asymmetric catalysis, which contrasts the resolution of racemic mixtures, has become of paramount importance, especially in pharmaceutical, agricultural, or food industry. To date, asymmetric catalysis is dominated by homogeneous catalysis because of its superior activity and selectivity as compared to heterogeneous catalysis.<sup>[1,2]</sup> On the other hand, heterogeneous catalysts promise increased stability and facilitated separation and recycling. As a consequence, substantial effort has been devoted to obtain catalytically active chiral surfaces, for instance by depos-

iting enantiopure molecules on achiral surfaces,<sup>[2-7]</sup> or by cutting achiral crystals along low-symmetry directions.<sup>[8,9]</sup> Another promising, yet largely unexplored, approach to achieve asymmetric heterogeneous catalysis is to employ surfaces of metals with chiral crystal structure.<sup>[10]</sup>

To rationally design catalysts for heterogeneous asymmetric catalysis, enantiospecific reactant-catalyst interactions and reaction pathways must be understood on the atomic scale. In this context, investigations of molecules deposited on well-defined surfaces with scanning tunneling microscopy (STM), temperature programmed desorption (TPD), or temperature-programmed X-ray photoelectron spectroscopy (TP-XPS) experiments under ultrahigh vacuum conditions have proven to be powerful methods. In particular, STM has been applied frequently to image enantiospecific reactant-catalyst interactions with submolecular resolution,<sup>[11-14]</sup> whereas reaction kinetics can be obtained from TPD and TP-XPS experiments. While TPD is an established method to determine enantiospecific reaction kinetics,<sup>[5,15]</sup> applications of TP-XPS have been limited to symmetric reactions so far.<sup>[16-20]</sup>

To date, the only surfaces of intrinsically chiral metals that have been characterized well enough to allow detailed investigations of atomic-scale reactant-catalyst interactions are the low-Miller index surfaces of intermetallic PdGa with 1:1 stoichiometry.<sup>[21]</sup> PdGa has recently attracted considerable attention as topological material hosting exotic fermionic quasiparticles<sup>[22,23]</sup> and as active and selective catalyst.<sup>[24,25]</sup> Owing to its

S. Stolz,<sup>[†]</sup> M. Danese, M. Di Giovannantonio,<sup>[††]</sup> J. I. Urgel,<sup>[†††]</sup> Q. Sun,<sup>[††††]</sup> A. Kinikar, M. Bommert, S. Mishra,<sup>[†††††]</sup> O. Gröning, D. Passerone, R. Widmer  
Nanotech@surfaces Laboratory  
Empa – Swiss Federal Laboratories for Materials Science and Technology  
Überlandstrasse 129, Dübendorf CH-8600, Switzerland  
E-mail: roland.widmer@empa.ch

S. Stolz, H. Brune  
Institute of Physics  
École Polytechnique Fédérale de Lausanne  
Lausanne CH-1015, Switzerland

 The ORCID identification number(s) for the author(s) of this article can be found under <https://doi.org/10.1002/adma.202104481>.

© 2021 The Authors. Advanced Materials published by Wiley-VCH GmbH. This is an open access article under the terms of the Creative Commons Attribution-NonCommercial-NoDerivs License, which permits use and distribution in any medium, provided the original work is properly cited, the use is non-commercial and no modifications or adaptations are made.

<sup>[†]</sup>Present address: Department of Physics, University of California, Berkeley, Berkeley, CA 94720, USA

<sup>[††]</sup>Present address: Istituto di Struttura della Materia – CNR (ISM-CNR), via Fosso del Cavaliere 100, Roma 00133, Italy

<sup>[†††]</sup>Present address: IMDEA Nanoscience, C/Faraday 9, Campus de Cantoblanco, Madrid 28049, Spain

<sup>[††††]</sup>Present address: Materials Genome Institute, Shanghai University, Shanghai 200444, China

<sup>[†††††]</sup>Present address: IBM Research – Zurich, Rüschlikon 8803, Switzerland

DOI: 10.1002/adma.202104481

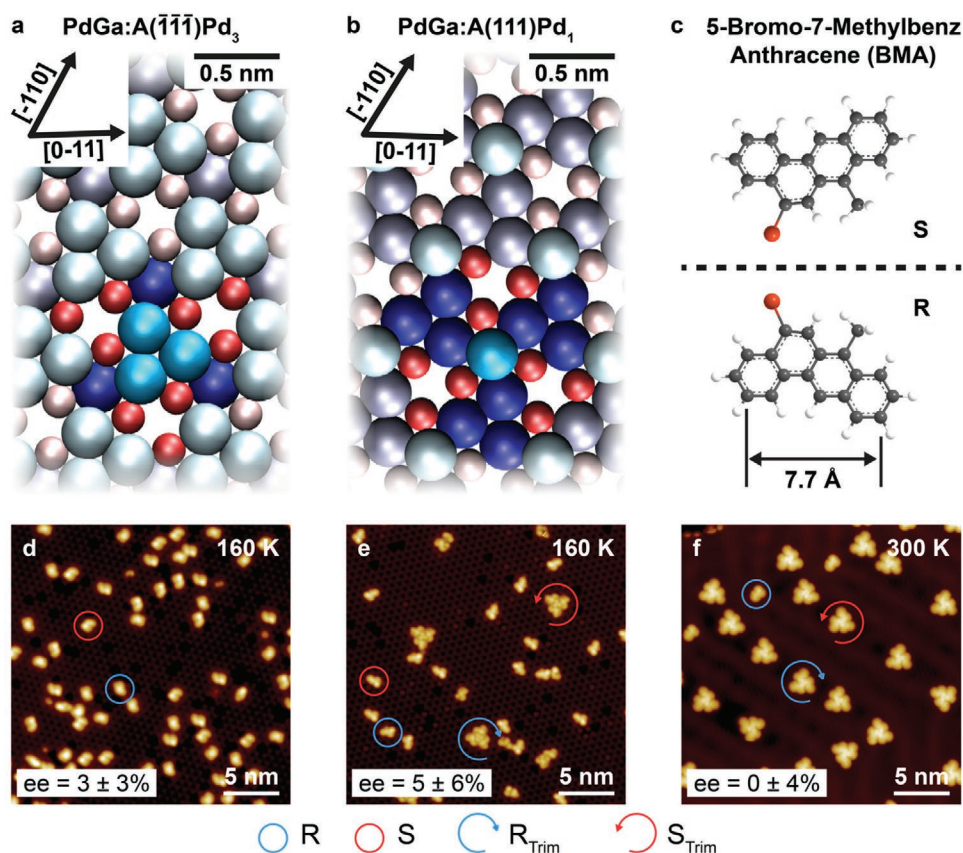


**Figure 1.** Model system for enantioselective debromination. a,b) Surface structure of the PdGa:A( $\bar{1}\bar{1}\bar{1}$ )Pd<sub>3</sub> surface (1st layer Pd<sub>3</sub> in bright blue; 2nd layer Ga<sub>3</sub> in red; 3rd layer Pd<sub>1</sub> in dark blue) (a) and the PdGa:A(111)Pd<sub>1</sub> (1st layer Pd<sub>1</sub> in bright blue; 2nd layer Ga<sub>3</sub> in red; 3rd layer Pd<sub>3</sub> in dark blue) (b). The chirality of both surfaces is highlighted with saturated colors for one top-layer Pd trimer (PdGa:A( $\bar{1}\bar{1}\bar{1}$ )Pd<sub>3</sub>) or Pd atom (PdGa:A(111)Pd<sub>1</sub>) and their neighboring Pd and Ga atoms in subjacent layers. c) Molecular structure of prochiral BMA, which occurs in two distinct surface enantiomers when confined to a planar configuration (Br red, C gray, H white). d–f) STM images of BMA on: d) PdGa:A( $\bar{1}\bar{1}\bar{1}$ )Pd<sub>3</sub> ( $V_{\text{Bias}} = 50$  mV;  $I_T = 50$  pA), e) PdGa:A(111)Pd<sub>1</sub> ( $V_{\text{Bias}} = -50$  mV;  $I_T = 100$  pA), and f) Au(111) ( $V_{\text{Bias}} = -50$  mV;  $I_T = 200$  pA). The respective deposition temperatures given in the images.

noncentrosymmetry, PdGa exists in two enantiomorphs that are denoted PdGa:A and PdGa:B.<sup>[26]</sup> Of particular interest are the two structurally different, threefold symmetric, chiral PdGa:A( $\bar{1}\bar{1}\bar{1}$ )Pd<sub>3</sub> (A: Pd<sub>3</sub> for short) and PdGa:A(111)Pd<sub>1</sub> (A: Pd<sub>1</sub>) surfaces (Figure 1a,b), which terminate by Pd trimers and isolated single Pd atoms, respectively.<sup>[27]</sup> These surfaces have proven to be excellent candidates to separate the geometric and electronic, i.e., ensemble and ligand, effect in heterogeneous catalysis<sup>[28–30]</sup> and to exhibit highly enantiospecific interaction with achiral and prochiral molecules.<sup>[13,14,31,32]</sup>

In this study, we employ the chiral PdGa{111} surfaces to quantitatively characterize thermally activated, enantioselective halogen elimination, which is the first step of several on-surface reactions, among others the frequently applied dehalogenative aryl–aryl coupling<sup>[33,34]</sup> that is for instance used to grow graphene nanoribbons<sup>[35–38]</sup> or extended 2D organic frameworks.<sup>[33,39–41]</sup> To date, the only attempts regarding asymmetric on-surface halogen elimination were reported by Rampulla et al. for chiral alkyl halides on low-symmetry copper surfaces.<sup>[42,43]</sup> They reported bromine elimination with an enantiomeric excess of up to 8% ± 4% for R-2-bromobutane on Cu(531).

Here, we investigate the thermally triggered asymmetric debromination of prochiral 5-bromo-7-methylbenz(a)anthracene

(BMA; Figure 1c) on the chiral PdGa{111} surfaces, and – as control experiment, where no enantioselective debromination is expected – on achiral Au(111). Enantioselectivity in this reaction is expressed in different debromination temperatures for the two surface enantiomers, which we study by means of TP-XPS, STM, and density functional theory (DFT).

## 2. Results and Discussion

For a conclusive discussion on the thermally activated debromination process, we first clarify the conditions under which BMA molecules remain pristine on the Au(111), A: Pd<sub>3</sub>, and A: Pd<sub>1</sub> surfaces. Adsorption of BMA on Au(111) shows no significant differences in the temperature range between 160 and 300 K, where the molecules remain intact on the surface. The molecules assemble into homochiral trimers, which appear in equal proportions with clockwise and counter-clockwise sense of rotations, i.e., there is no significant excess of surface enantiomers  $ee_{\text{BMA}} = 0\% \pm 4\%$ , which is defined as  $ee_{\text{BMA}} = 100\% \times \frac{\#R - \#S}{\#R + \#S}$  (Figure 1f; and Figure S6, Supporting Information).

BMA has been deposited at 160 K on the PdGa{111} surfaces to avoid debromination. On A: Pd<sub>3</sub>, pristine BMA molecules

appear as isolated monomers (Figure 1d; and Figure S8, Supporting Information) in two distinct configurations, each present in three rotationally equivalent forms. The STM signatures of these two distinct configurations resemble trapezoids that are mirrored one with respect to the other (Figure S9, Supporting Information) and are thus assigned to R and S BMA enantiomers that form a racemic mixture, i.e.,  $ee_{\text{BMA}} = 3\% \pm 3\%$ .

On A:Pd<sub>1</sub>, BMA molecules deposited at 160 K appear in seven different configurations, five of which are isolated monomers occurring in three rotationally equivalent geometries, and two are homochiral trimer assemblies with opposing sense of rotation (Figure 1e; and Figures S14–S17, Supporting Information). All monomers exhibit a trapezoid-like shape (Figure S15, Supporting Information), based on which we conduct the assignment that is experimentally confirmed with nc-AFM (Figure S16, Supporting Information) to R and S enantiomers. No significant enantiomeric excess ( $ee_{\text{BMA}} = 5\% \pm 6\%$ ) is determined for these low-temperature adsorption conditions of BMA in A:Pd<sub>1</sub>.

By superimposing the surface atomic and the BMA molecular structure onto STM images, the exact adsorption geometry of both BMA surface enantiomers on the A:Pd<sub>3</sub> and A:Pd<sub>1</sub> surfaces can be identified. The most important difference between the adsorption geometries of BMA surface enantiomers on A:Pd<sub>3</sub> is that for R BMA the bromine is atop a single Pd atom in the third layer, whereas for S BMA it lies above the center of the Ga trimers in the second layer (Figure 2c,f). The experimentally determined adsorption geometries are identical to the most favorable ones derived with DFT calculations with corresponding adsorption energies of  $E_{\text{AdsR}} = -2.866$  eV and  $E_{\text{AdsS}} = -2.827$  eV for the R and S BMA, respectively (Table S3 and Figure S10, Supporting Information). Furthermore, the comparison of the DFT simulated STM images with the experimental STM signatures confirms the assignment of the surface enantiomers and their respective adsorption sites (Figure 2a,b,d,e).

Analogous to BMA adsorbed on A:Pd<sub>3</sub>, we identify the adsorption geometries of all BMA configurations on A:Pd<sub>1</sub> from STM images, which are discussed in detail in Note 5 in the Supporting Information. The energetically most favorable adsorption geometries derived from DFT calculations coincide with the ones observed experimentally. The respective adsorption energies determined with DFT differ by no more than 20 meV (Table S4, Supporting Information). Also the experimental STM signatures of BMA monomers are in very good agreement with the ones obtained from DFT simulations and thus again validate the assignment of the surface enantiomers. For the most frequently observed R and S BMA monomer configurations on A:Pd<sub>1</sub>, shown in Figure 2i,l, the bromine atom lies on a top-layer Pd atom in both cases. Slight differences in adsorption geometries of R and S enantiomers arise with respect to subjacent layers due to the chirality of the surface.

Having established that on Au(111), A:Pd<sub>3</sub>, and A:Pd<sub>1</sub> surfaces pristine BMA appear as racemic mixture, the dynamics of BMA debromination are investigated with TP-XPS for the Au(111) and PdGa{111} surfaces with heating rates of 0.1 and 0.05 K s<sup>-1</sup>, respectively (Figure 3). On all three surfaces similar changes of the chemical state of the Br 3d doublet, shown in Figure 3a–c, are observed in the TP-XPS maps. In a first step, bromine detaches from the molecule and chemisorbs

on the surface, which is expressed in a distinct chemical shift of the Br 3d doublet to lower binding energies. Second, bromine desorbs, resulting in an overall intensity decrease of the Br 3d signal. Highlighted by the temperature-dependent relative intensity (Figure 3d) for both chemical states of bromine, i.e., bromine attached to the molecule (Br–C) and bromine adsorbed on the surface (Br–Au/Br–Pd), the temperature range and line shape for the transitions varies significantly between the three investigated substrates. Considering a rigid shift of about 11 K to higher temperatures due to the larger heating rate for Au(111) (Figure S3, Supporting Information), BMA debromination occurs between 300 and 400 K on Au(111), but already takes place between 200 and 290 K and between 200 and 300 K for the Pd<sub>3</sub>- and Pd<sub>1</sub>-terminated PdGa{111} surfaces, respectively. On the other hand, bromine has entirely desorbed at 460 K from Au(111), while on PdGa{111} this process is only initiated at 470 K and requires a temperature of 550 K to be entirely desorbed.

In the following, we focus on the temperature evolution of the bromine elimination process by scrutinizing the TP-XPS intensity profiles of Br–C, which are shown in Figure 4a. Br–C not only decreases in a dissimilar temperature range on Au(111), A:Pd<sub>3</sub>, and A:Pd<sub>1</sub>, but it also exhibits a different kinetics. In particular, the Br–C signal declines in a sigmoidal shape for Au(111), in a rather linear shape for A:Pd<sub>3</sub>, and a double-sigmoidal shape for A:Pd<sub>1</sub>.

For a more quantitative assessment of the debromination kinetics, we derive for each BMA surface enantiomer the mean debromination temperature, i.e., the temperature at which half of the respective surface enantiomers debrominated, from TP-XPS by fitting the fraction of intact BMA molecule at any given temperature with an error function, as discussed in Note 1 in the Supporting Information. Fitting the Br–C with Equation (S1) (Supporting Information), shown as solid areas in Figure 4a,e,j, yields absolute differences in debromination temperatures of  $\Delta T_{\text{Au111}} = 0$  K,  $\Delta T_{\text{Pd}_3} = 36$  K, and  $\Delta T_{\text{Pd}_1} = 46$  K between the BMA surface enantiomers on Au(111), A:Pd<sub>3</sub>, and A:Pd<sub>1</sub>, respectively. These temperature differences clearly show that BMA debromination occurs without enantioselectivity on Au(111), but highly asymmetric on the chiral PdGa{111} surfaces.

In the following, the conclusions drawn from fitting the Br–C traces with Equation (S1) (Supporting Information) are complemented by STM (cf. Figure 4). As shown in Figure 4c, after heating to 350 K the molecules partially debrominate and we find a racemic mixture of BMA monomers ( $ee_{\text{BMA}} = 1\% \pm 8\%$ ) and BMA dimers ( $ee_{\text{Dimer}} = 100\% \frac{|\#RR - \#SS|}{\#RR + \#RS + \#SS} = 5\% \pm 5\%$ ;

YZ dimers consist of one Y = {R,S} and one Z = {R,S} debrominated BMA surface enantiomer, cf. Figure S7, Supporting Information). Upon annealing to 400 K all BMA are debrominated and covalent coupling between BMA dimers is frequently observed – a structure of four merged dimers is indicated by a white arrow in Figure 4d. All of the formed molecular structures occur as racemic mixture on the Au(111) surface.

Asymmetric bromine elimination for BMA on A:Pd<sub>3</sub> is corroborated with TP-XPS, as Br–C decreases to 50% of its initial value and then remains constant, if the substrate temperature is kept slightly above the onset of the reaction process (Figure S11

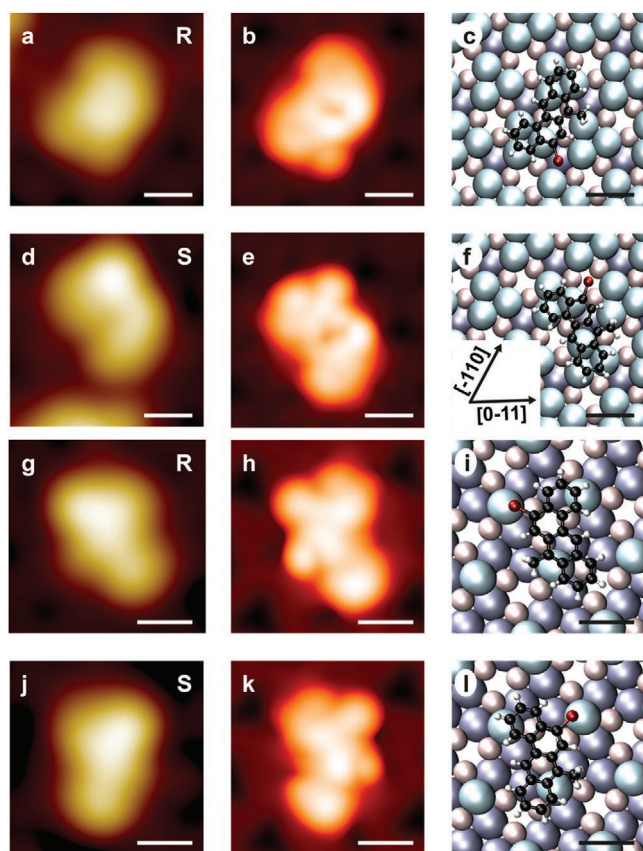


**Figure 2.** Adsorption geometries. Experimental STM images of the R (a,g) and the S (d,j) BMA surface enantiomer on the PdGa:A( $\bar{1}\bar{1}\bar{1}$ )Pd<sub>3</sub> (PdGa:A(111)Pd<sub>1</sub>) surface with the corresponding DFT-calculated STM images in (b,h) and (e,k) and adsorption geometries in (c,i) and (f,l). All scale bars correspond to 0.5 nm.

and S12, Supporting Information). STM investigations shown in Figure 4f–i further support this finding. Below 250 K (Figure 4g), all S BMA enantiomers debrominate and, with more than 90% probability, subsequently dimerize in numerous different configurations (Figure S13, Supporting Information), while most R BMA persist unaltered with a coverage of about 50% relative to all BMA derived molecular structures (Figure 4i). Upon further heating to 300 K, also R BMA debrominate and dimerize in different configurations, as shown in Figure 4h.

STM investigations also confirm enantioselective BMA debromination on A:Pd<sub>1</sub>, as of the initial racemic mixture at 160 K (Figure 4k) only S enantiomers remain brominated between 225 and 250 K (Figure 4l) with a coverage relative to all BMA molecular structures of almost 50% (Figure 4n). Debrominated BMA on A:Pd<sub>1</sub> mostly occur isolated (Figure 4l and Figures S14 and S18–S20, Supporting Information) after annealing at 250 K. The few dimer-like agglomerates present at this stage appear with an  $ee_{\text{Dimer}} = 75\%_{-25\%}^{+17\%}$  in favor of RR (Figure S21, Supporting Information). Upon annealing to 300 K, S BMA debrominate and can form dimer-like RS and SS agglomerates, thus eliminating any enantiomeric excess for dimer-like agglomerates (Figure 4m).

Based on the experimentally observed enantioselective debromination, we can deduce several aspects of the reaction kinetics. Specifically, the conversion of pristine R into S BMA and vice-versa is suppressed on both PdGa{111} surfaces at least up to the debromination temperature of the less stable BMA surface enantiomer. Interestingly, the onset temperatures for the debromination process on PdGa{111} correspond well to those reported for Cu(111).<sup>[20,44]</sup> This observation supports the presumption that these surfaces have a comparable catalytic activity due to the similar average energy of d-band electrons (d-band center).<sup>[27,45,46]</sup> An intriguing difference is that on PdGa{111} surfaces the BMA debromination occurs over a

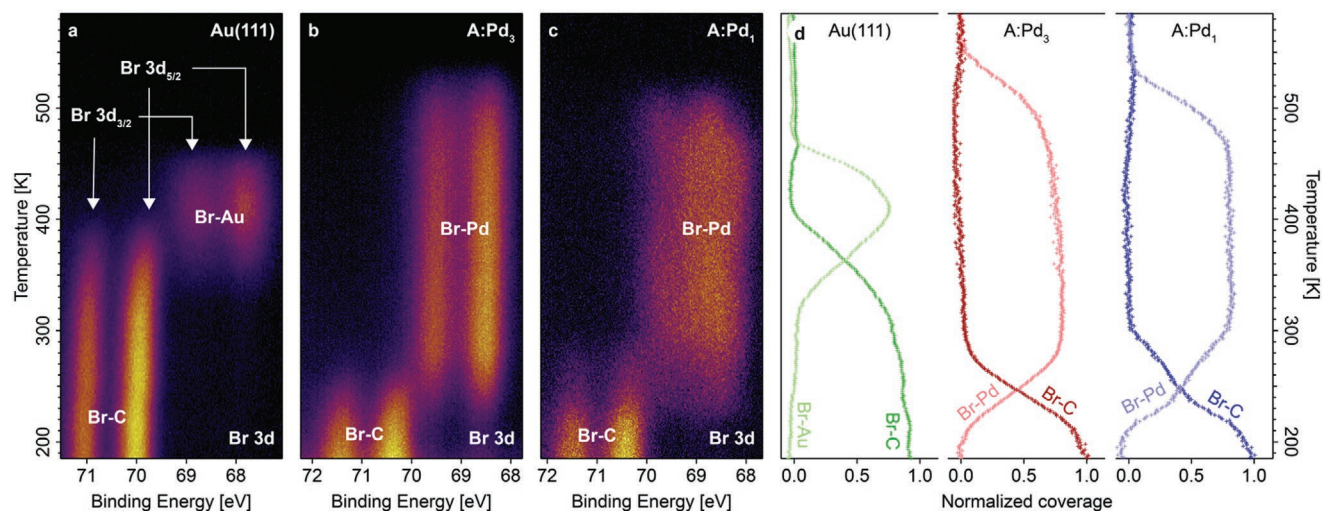


**Figure 3.** Bromine detachment and desorption. a–c) TP-XPS maps of the Br 3d core level doublet for BMA adsorbed on Au(111) (a), PdGa:A( $\bar{1}\bar{1}\bar{1}$ )Pd<sub>3</sub> (b), and PdGa:A(111)Pd<sub>1</sub> (c). d) Temperature dependence of the Br–C and Br–Au/Br–Pd components extracted from the Br 3d TP-XPS maps and normalized to the initial bromine signal for Au(111) (left, heating rate  $r = 0.1 \text{ K s}^{-1}$ ), PdGa:A( $\bar{1}\bar{1}\bar{1}$ )Pd<sub>3</sub> (center,  $r = 0.05 \text{ K s}^{-1}$ ), and PdGa:A(111)Pd<sub>1</sub> (right,  $r = 0.05 \text{ K s}^{-1}$ ).

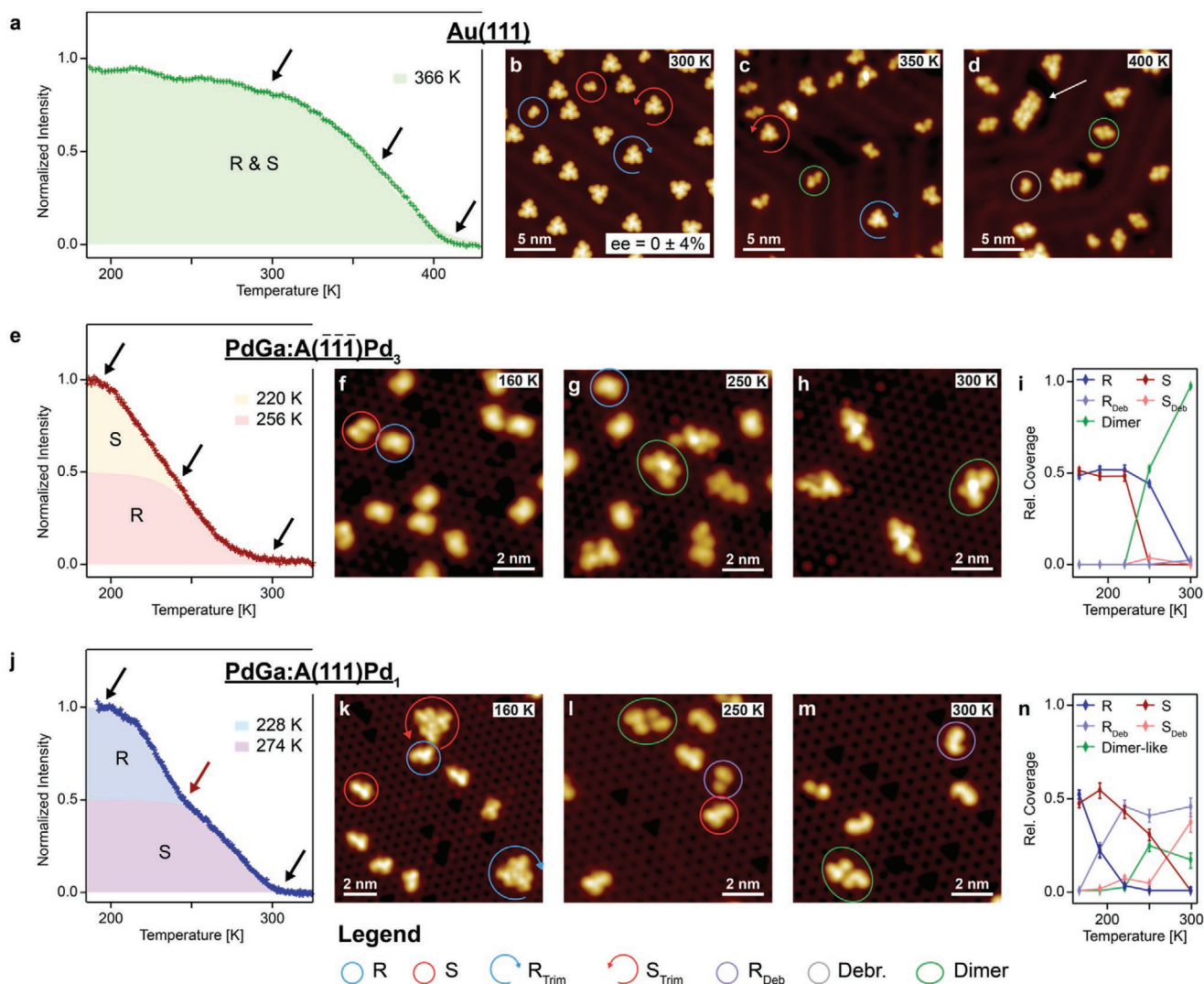


**Figure 4.** Enantioselectivity of BMA debromination. a,e,j) Br–C intensity for the Au(111) (a), PdGa:A( $\bar{1}\bar{1}\bar{1}$ )Pd<sub>3</sub> (e), and PdGa:A(111)Pd<sub>1</sub> (j) surfaces. The shaded areas beneath each curve show fits with Equation (S1) (Supporting Information); the contribution of each BMA surface enantiomer, with the enantiomeric form as determined from STM, is displayed in a different color. The temperatures at which half of the respective surface enantiomer is debrominated are given in the legend. The arrows indicate the state of debromination visualized in the STM images in (b–d), (f–h), and (k–m). b–d) STM images of BMA on Au(111) deposited at 300 K (b) and after subsequent annealing at 350 K (c) and at 400 K (d). f–h) STM images of BMA on PdGa:A( $\bar{1}\bar{1}\bar{1}$ )Pd<sub>3</sub> deposited at 160 K (f) and after subsequent heating to 250 K (g) and to 300 K (h). i) The abundance of BMA species on PdGa:A( $\bar{1}\bar{1}\bar{1}$ )Pd<sub>3</sub>, which has been determined based on STM images that have been recorded after annealing to a certain temperature. k–n) STM images of BMA on PdGa:A( $\bar{1}\bar{1}\bar{1}$ )Pd<sub>3</sub> deposited at 165 K (k) and after subsequent annealing to 250 K (l) and 300 K (m). n) The abundance of BMA species on PdGa:A(111)Pd<sub>1</sub>, which has been determined based on STM images recorded after the annealing process. STM parameters: b–d,k–m)  $V_{\text{Bias}} = -50$  mV, f–h)  $V_{\text{Bias}} = 50$  mV; b,d,f,k,m)  $I_T = 200$  pA, c)  $I_T = 20$  pA, g,h)  $I_T = 50$  pA.

wider temperature range than on Cu(111).<sup>[20,44]</sup> The temperature range for debromination is particularly wide on Au(111), which has been attributed to reversible debromination processes.<sup>[19,20]</sup> Therefore we simulate the debromination reaction on the PdGa{111} surfaces with a rate equation model including reversibility and enantiospecific energy barriers. We simplify the model by assuming the enantiospecific reaction paths to differ only with regard to the debromination energy of the BMA surface enantiomers (Figure S2 and Note 2 in the Supporting Information) and determine energy barrier differences for the debromination of the BMA surface enantiomers of 0, 40, and 55 meV on Au(111), A:Pd<sub>3</sub>, and A:Pd<sub>1</sub>, respectively.

According to two empirical principles, which are generally valid for a large class of reactions, we can infer trends on the reaction rates and thereby on the origin of the enantioselective debromination, without knowing the precise reaction pathway. First, the Bell–Evans–Polanyi (BEP) principle relates a larger adsorption energy difference of the initial and final reaction state (i.e., the pristine and debrominated BMA, respectively) to a reduced activation barrier and thereby to higher reaction rates. Second, according to the Hammond–Leffler postulate, close proximity of the adsorption configuration of the final state relative to that of the pristine molecule can yield higher reaction rates, too. Using DFT simulations

we have found that in all cases there are stable final state configurations in close structural proximity of the pristine BMA (Figure S24, Supporting Information). In the case of A:Pd<sub>1</sub>, we see no substantial difference in the adsorption energy of the pristine R and S enantiomer, but a 120 meV lower energy of the debrominated R BMA over the S surface enantiomer. According to the BEP principle we would therefore expect the activation barrier for the R enantiomer to be lower, which agrees with the experiment. For the A:Pd<sub>3</sub> surface, the initial–final state energy difference between the R and the S enantiomers are very similar and differ by only 31 meV (cf. Figure S23, Supporting Information). This is about 1% of the reactant adsorption energy and most probably beyond the precision of the DFT calculations.<sup>[47]</sup> Therefore, DFT calculations on A:Pd<sub>3</sub> remain nonconclusive on the origin of the experimentally observed selectivity toward the S enantiomer. Consequently, we find that although DFT successfully predicts the correct adsorption configurations of the initial and final state, the accuracy is insufficient to capture the origin of the experimentally observed highly asymmetric halogen elimination. The latter would require computational methods that accurately access the free energy landscape and take into account several reaction pathways for both surface enantiomers on the complex and corrugated PdGa{111}.

### 3. Conclusion

We have demonstrated that the halogen elimination process of prochiral BMA proceeds enantioselectively with unprecedentedly high differences in debromination temperatures of 36 K and even 46 K between the two surface enantiomers on the Pd<sub>3</sub>- and Pd<sub>1</sub>-terminated PdGa{111} surfaces, respectively. Such high temperature differences allow asymmetric halogen elimination with an enantiomeric excess of more than 90%. Moreover, the observation that on Pd<sub>3</sub>- and Pd<sub>1</sub>-terminated PdGa{111} surfaces of the same enantiomorph the opposite BMA surface enantiomer debrominates at lower temperatures evidences a strong ensemble effect and emphasizes the significance of the atomic details of the entire molecule-substrate system. The enantioselective halogen elimination demonstrates the strong chiral recognition of the PdGa{111} surfaces and highlights the immense potential of intrinsically chiral crystals in asymmetric catalysis.

### Supporting Information

Supporting Information is available from the Wiley Online Library or from the author.

### Acknowledgements

The authors acknowledge funding from the Swiss National Science Foundation under SNSF Project Nos. 159690, 175923, and 51NF40-182892 (NCCR MARVEL). The XPS experiments were performed on the X03DA (PEARL) beamline at the Swiss Light Source, Paul Scherrer Institut, Villigen, Switzerland. The authors also thank the beamline manager Dr. Matthias Muntwiler (PSI) for his technical support. For

computational resources, the authors acknowledge the Swiss National Supercomputing Centre.

Open access funding provided by ETH-Bereich Forschungsanstalten.

### Conflict of Interest

The authors declare no conflict of interest.

### Author Contributions

R.W. and O.G. conceived and initiated the project in collaboration with H.B. S.S. performed the STM and nc-AFM experiments under supervision of R.W. S.S., M.D.G., J.I.U., Q.S., A.K., M.B., S.M. and R.W. performed the XPS measurements. M.D. conducted DFT simulations under supervision of D.P. S.S. analyzed all experimental data and assisted M.D. and D.P. in the analysis of DFT calculations. S.S. wrote the manuscript with input from all co-authors.

### Data Availability Statement

The data that support the findings of this study are openly available in Materials Cloud Archive at <http://doi.org/10.24435/materialscloud:pm-8p>.

### Keywords

asymmetric catalysis, chiral materials, intermetallic compounds, surface chemistry, surface enantiomers

Received: June 11, 2021

Revised: September 19, 2021

Published online: November 11, 2021

- [1] M. Heitbaum, F. Glorius, I. Escher, *Angew. Chem., Int. Ed.* **2006**, *45*, 4732.
- [2] G. Kyriakou, S. K. Beaumont, R. M. Lambert, *Langmuir* **2011**, *27*, 9687.
- [3] D. Stacchiola, L. Burkholder, W. T. Tysoe, *J. Am. Chem. Soc.* **2002**, *124*, 8984.
- [4] I. Lee, F. Zaera, *J. Am. Chem. Soc.* **2006**, *128*, 8890.
- [5] F. Gao, Y. Wang, Z. Li, O. Furlong, W. T. Tysoe, *J. Phys. Chem. C* **2008**, *112*, 3362.
- [6] D. J. Watson, R. J. Bennie Ram John Jesudason, S. K. Beaumont, G. Kyriakou, J. W. Burton, R. M. Lambert, *J. Am. Chem. Soc.* **2009**, *131*, 14584.
- [7] T. J. Lawton, V. Pushkarev, D. Wei, F. R. Lucci, D. S. Sholl, A. J. Gellman, E. C. H. Sykes, *J. Phys. Chem. C* **2013**, *117*, 22290.
- [8] C. F. McFadden, P. F. Cremer, A. J. Gellman, *Langmuir* **1996**, *12*, 2483.
- [9] D. S. Sholl, A. J. Gellman, *AIChE J.* **2009**, *55*, 2484.
- [10] N. Shukla, A. J. Gellman, *Nat. Mater.* **2020**, *19*, 939.
- [11] V. Demers-Carpentier, G. Goubert, F. Masini, R. Lafleur-Lambert, Y. Dong, S. Lavoie, G. Mahieu, J. Boukouvalas, H. Gao, A. M. H. Rasmussen, L. Ferrighi, Y. Pan, B. Hammer, P. H. McBreen, *Science* **2011**, *334*, 776.
- [12] G. Goubert, Y. Dong, M. N. Groves, J.-C. Lemay, B. Hammer, P. H. McBreen, *Nat. Chem.* **2017**, *9*, 531.
- [13] J. Prinz, O. Gröning, H. Brune, R. Widmer, *Angew. Chem., Int. Ed.* **2015**, *54*, 3902.

- [14] S. Stolz, A. V. Yakutovich, J. Prinz, T. Dienel, C. A. Pignedoli, H. Brune, O. Gröning, R. Widmer, *Angew. Chem., Int. Ed.* **2020**, *59*, 18179.
- [15] A. J. Gellman, Y. Huang, X. Feng, V. V. Pushkarev, B. Holsclaw, B. S. Mhatre, *J. Am. Chem. Soc.* **2013**, *135*, 19208.
- [16] K. A. Simonov, N. A. Vinogradov, A. S. Vinogradov, A. V. Generalov, E. M. Zagrebina, N. Mårtensson, A. A. Cafolla, T. Carpy, J. P. Cunniffe, A. B. Preobrajenski, *J. Phys. Chem. C* **2014**, *118*, 12532.
- [17] M. Di Giovannantonio, M. Tomellini, J. Lipton-Duffin, G. Galeotti, M. Ebrahimi, A. Cossaro, A. Verdini, N. Kharche, V. Meunier, G. Vasseur, Y. Fagot-Revurat, D. F. Perepichka, F. Rosei, G. Contini, *J. Am. Chem. Soc.* **2016**, *138*, 16696.
- [18] M. Di Giovannantonio, O. Deniz, J. I. Urgel, R. Widmer, T. Dienel, S. Stolz, C. Sánchez-Sánchez, M. Muntwiler, T. Dumsclaff, R. Berger, A. Narita, X. Feng, K. Müllen, P. Ruffieux, R. Fasel, *ACS Nano* **2018**, *12*, 74.
- [19] M. Fritton, D. A. Duncan, P. S. Deimel, A. Rastgoo-Lahrood, F. Allegretti, J. V. Barth, W. M. Heckl, J. Björk, M. Lackinger, *J. Am. Chem. Soc.* **2019**, *141*, 4824.
- [20] S. Stolz, M. Di Giovannantonio, J. I. Urgel, Q. Sun, A. Kinikar, G. Borin Barin, M. Bommert, R. Fasel, R. Widmer, *Angew. Chem., Int. Ed.* **2020**, *59*, 14106.
- [21] M. Armbrüster, H. Borrmann, M. Wedel, Y. Prots, R. Giedigkeit, P. Gille, Z. Kristallogr, *NCS* **2010**, *225*, 617.
- [22] N. B. M. Schröter, S. Stolz, K. Manna, F. de Juan, M. G. Vergniory, J. A. Krieger, D. Pei, T. Schmitt, P. Dudin, T. K. Kim, C. Cacho, B. Bradlyn, H. Borrmann, M. Schmidt, R. Widmer, V. N. Strocov, C. Felser, *Science* **2020**, *369*, 179.
- [23] P. Sessi, F.-R. Fan, F. Küster, K. Manna, N. B. M. Schröter, J.-R. Ji, S. Stolz, J. A. Krieger, D. Pei, T. K. Kim, P. Dudin, C. Cacho, R. Widmer, H. Borrmann, W. Shi, K. Chang, Y. Sun, C. Felser, S. S. P. Parkin, *Nat. Commun.* **2020**, *11*, 3507.
- [24] M. Armbrüster, K. Kovnir, M. Behrens, D. Teschner, Y. Grin, R. Schlögl, *J. Am. Chem. Soc.* **2010**, *132*, 14745.
- [25] Q. Yang, G. Li, K. Manna, F. Fan, C. Felser, Y. Sun, *Adv. Mater.* **2020**, *32*, 1908518.
- [26] D. Rosenthal, R. Widmer, R. Wagner, P. Gille, M. Armbrüster, Y. Grin, R. Schlögl, O. Gröning, *Langmuir* **2012**, *28*, 6848.
- [27] J. Prinz, R. Gaspari, C. A. Pignedoli, J. Vogt, P. Gille, M. Armbrüster, H. Brune, O. Gröning, D. Passerone, R. Widmer, *Angew. Chem.* **2012**, *124*, 9473.
- [28] W. M. H. Sachtler, *Catal. Rev.: Sci. Eng.* **1976**, *14*, 193.
- [29] J. K. Nørskov, T. Bligaard, B. Hvolbæk, F. Abild-Pedersen, I. Chorkendorff, C. H. Christensen, *Chem. Soc. Rev.* **2008**, *37*, 2163.
- [30] J. Prinz, R. Gaspari, Q. S. Stöckl, P. Gille, M. Armbrüster, H. Brune, O. Gröning, C. A. Pignedoli, D. Passerone, R. Widmer, *J. Phys. Chem. C* **2014**, *118*, 12260.
- [31] S. Stolz, O. Gröning, J. Prinz, H. Brune, R. Widmer, *Proc. Natl. Acad. Sci. USA* **2020**, *117*, 14838.
- [32] S. Stolz, M. Bauer, C. A. Pignedoli, N. Krane, M. Bommert, E. Turco, N. Bassi, A. Kinikar, N. Merino-Diez, R. Hany, H. Brune, O. Gröning, R. Widmer, *Commun. Chem.* **2021**, *4*, 51.
- [33] L. Grill, M. Dyer, L. Lafferentz, M. Persson, M. V. Peters, S. Hecht, *Nat. Nanotechnol.* **2007**, *2*, 687.
- [34] S. Clair, D. G. de Oteyza, *Chem. Rev.* **2019**, *119*, 4717.
- [35] J. Cai, P. Ruffieux, R. Jaafar, M. Bieri, T. Braun, S. Blankenburg, M. Muoth, A. P. Seitsonen, M. Saleh, X. Feng, K. Müllen, R. Fasel, *Nature* **2010**, *466*, 470.
- [36] P. Ruffieux, S. Wang, B. Yang, C. Sánchez-Sánchez, J. Liu, T. Dienel, L. Talirz, P. Shinde, C. A. Pignedoli, D. Passerone, T. Dumsclaff, X. Feng, K. Müllen, R. Fasel, *Nature* **2016**, *531*, 489.
- [37] O. Gröning, S. Wang, X. Yao, C. A. Pignedoli, G. Borin Barin, C. Daniels, A. Cupo, V. Meunier, X. Feng, A. Narita, K. Müllen, P. Ruffieux, R. Fasel, *Nature* **2018**, *560*, 209.
- [38] D. J. Rizzo, G. Veber, T. Cao, C. Bronner, T. Chen, F. Zhao, H. Rodriguez, S. G. Louie, M. F. Crommie, F. R. Fischer, *Nature* **2018**, *560*, 204.
- [39] K. J. Shi, Zhang, C. H. Shu, D. Y. Li, X. Y. Wu, P. N. Liu, *Chem. Commun.* **2016**, *52*, 8726.
- [40] C. Steiner, J. Gebhardt, M. Ammon, Z. Yang, A. Heidenreich, N. Hammer, A. Görling, M. Kivala, S. Maier, *Nat. Commun.* **2017**, *8*, 14765.
- [41] G. Galeotti, F. De Marchi, E. Hamzehpoor, O. MacLean, M. Rajeswara Rao, Y. Chen, L. V. Besteiro, D. Dettmann, L. Ferrari, F. Frezza, P. M. Sheverdyeva, R. Liu, A. K. Kundu, P. Moras, M. Ebrahimi, M. C. Gallagher, F. Rosei, D. F. Perepichka, G. Contini, *Nat. Mater.* **2020**, *19*, 874.
- [42] D. M. Rampulla, A. J. Francis, K. S. Knight, A. J. Gellman, *J. Phys. Chem. B* **2006**, *110*, 10411.
- [43] D. M. Rampulla, A. J. Gellman, *Surf. Sci.* **2006**, *600*, 2823.
- [44] K. A. Simonov, N. A. Vinogradov, A. S. Vinogradov, A. V. Generalov, E. M. Zagrebina, G. I. Svirskiy, A. A. Cafolla, T. Carpy, J. P. Cunniffe, T. Taketsugu, A. Lyalin, N. Mårtensson, A. B. Preobrajenski, *ACS Nano* **2015**, *9*, 8997.
- [45] X. Bian, Q. Wang, X. Wang, L. Wang, W.-Q. Li, G.-H. Chen, H. Zhu, *RSC Adv.* **2016**, *6*, 74973.
- [46] J. K. Nørskov, T. Bligaard, J. Rossmeisl, C. H. Christensen, *Nat. Chem.* **2009**, *1*, 37.
- [47] A. V. Yakutovich, J. Hoja, D. Passerone, A. Tkatchenko, C. A. Pignedoli, *J. Am. Chem. Soc.* **2018**, *140*, 1401.